Analyst

ROYAL SOCIETY OF CHEMISTRY

PAPER

View Article Online
View Journal | View Issue

Cite this: *Analyst*, 2026, **151**, 458

Hydrazine oxidation on a single electrocatalytic nanoring

Sakshi A. Ailawar, †[a] Guillermo Colón-Quintana,†[a] Thomas B. Clarke[b] and Jeffrey E. Dick *[a,c]

Gold nanoring electrodes were fabricated through an electrochemical deposition method involving a gold chloride solution within an oil droplet at the interface of an aqueous supporting electrolyte phase. The electrochemical oxidation of hydrazine in an alkaline medium was studied *via* cyclic voltammetry and compared to that of a traditional gold macroelectrode. The nanoring electrode produced a well-defined cyclic voltammogram response with a similarly negative onset potential and higher current density, attributed to the combined effects of gold's catalytic activity and the nanoring geometry, which promotes radial diffusion. COMSOL Multiphysics simulations were performed to model the hydrazine oxidation process and capture the influence of electrode geometry on current response. The simulations showed strong agreement with the experimental data, validating the role of geometry-influenced mass transport in shaping the CV features. This study demonstrates that gold nanorings can generate interpretable and reproducible electrochemical signatures for hydrazine oxidation. The integration of experimental and computational approaches highlights how nanoscale geometry influences electrochemical performance and provides insights into structure–activity relationships in catalytic systems.

Received 16th June 2025,
Accepted 13th October 2025

DOI: 10.1039/d5an00651a

rsc.li/analyst

1. Introduction

Hydrazine (N_2H_4) has been studied for a long time for its high energy density and clean decomposition products. Its electrochemical oxidation, which produces nitrogen gas without emitting CO_2, has gained significant attention for sustainable energy technologies, including hydrogen production.[1–6] Bard *et al*. investigated the effect on the oxidation of hydrazine in aqueous solutions when a platinum electrode was pre-treated using chronopotentiometry. As hydrazine is one of the most popular reducing agents, hydrazine oxidation was studied in alkaline media on various metal electrodes like nickel,[7,8] cobalt,[9,10] gold,[11–16] platinum,[17–19] palladium,[10,12] silver[16,20] and mercury.[16,21]

Asazawa *et al.* studied the oxidation of hydrazine and its derivatives on different polycrystalline metal electrodes in an alkaline medium and reported the lower onset potential value for cobalt and nickel compared to platinum.[22] Gold electrodes have gathered significant attention due to their excellent conductivity, chemical stability, and high electrocatalytic activity of gold nanoparticles, which are important for reliable electrochemical reactions and sensing.[23,24] The electrochemical oxidation is further influenced by the geometry of the electrode, surface characteristics, surface oxides and the surrounding electrochemical environmental.[25–29]

Among various nanostructured electrodes, nanoring geometry offers advantages due to its high aspect ratio and the curved geometry.[30–32] These features enhance mass transport and provide a high density of active sites, which can confine reactants and accelerate the reaction kinetics. Compared to other nanoscale geometries like nano-band or nano-disks, nanorings demonstrate a superior performance, achieving lower onset potential and higher current densities for hydrazine oxidation.[15,33,34] Integrating this knowledge with computational modelling tools, such as COMSOL Multiphysics, has further advanced the understanding of electrochemical processes at nanostructured electrodes.[35,36] Simulations provide insights into the distribution of electric fields, concentration gradients, and reaction intermediates, enabling the optimization of electrode designs for maximum efficiency.

In this study, we focus on fabrication and characterization of gold nanoring electrodes for the electrochemical oxidation of hydrazine in alkaline medium. Building on our previous work on gold ring arrays,[37–39] we take advantage of the nanoring geometry and study the relationship between electrocatalytic performance and the electrode geometry. Additionally, we perform COMSOL Multiphysics simulations to

---

[a] *Department of Chemistry, Purdue University, West Lafayette, IN 47907, USA. E-mail: jdick@purdue.edu*
[b] *Department of Chemistry, Northwestern University, Evanston, IL 60208, USA*
[c] *Elmore Family School of Electrical and Computer Engineering, Purdue University, West Lafayette, IN 47907, USA*

† These authors contributed equally to this work.

model the electrochemical environment and validate experimental findings.

2. Results and discussion

2.1. Deposition of the gold nanoring

In this experiment, we electrochemically deposited a single gold nanoring using a sub-microliter droplet of gold(III) chloride dissolved in the oil phase, submerged in an aqueous supporting electrolyte phase. Specifically, a 0.2 μL droplet of 10 mM gold chloride dissolved in 100 mM tetrabutylammonium perchlorate (TBAP) and 1,2-dichloroethane (DCE) was pipetted onto a clean indium tin oxide (ITO) substrate with an electroactive area of radius 1.5 mm, placed in an acrylic cell. A solution of 1 M potassium chloride was used as the supporting electrolyte solution. The three-electrode system was used, as shown in Fig. 1a, consisting of the working electrode (ITO), thin glassy carbon counter electrode, and a salt bridge connected to the Ag|AgCl reference electrode. A reductive potential was applied to electrodeposit gold at the interface of the oil droplet on the ITO. Chronoamperometry was employed, where the potential was stepped from −0.65 V for 0.5 s to 0.3 V for 0.5 s and cycled twice between these potentials (Fig. S1). The potential of −0.65 V was sufficient to reduce the chloroaurate ion to gold. These potentials facilitated fast nucleation of gold metal followed by slow growth to induce ring formation dynamics.[37] After deposition, the aqueous solution was carefully decanted, and the ITO surface was rinsed with ultrapure water to remove residual KCl. This was followed by rinsing with ethanol to remove residual water and aid drying. Finally, DCE was used to dissolve and remove any remaining salts, including TBAP and gold(III) chloride. These experiments resulted in continuous single nanoring deposition, which was confirmed by scanning electron microscopy (SEM) images (Fig. S2). Energy-dispersive X-ray spectroscopy (EDS) verified the presence of gold (Fig. S3). The thickness of the ring was observed to be 133.75 nm, and the radius was 379.65 μm from the SEM image. The short electrodeposition duration and protective gold nanoring layer minimize the ITO degradation, as confirmed by post-deposition SEM imaging showing no significant morphological changes.[40–42]

2.2. Hydrazine oxidation on the working electrodes

To study the electrochemical activity of the electrodes, we prepared a solution of 10 mM hydrazine in 250 mM potassium hydroxide. The solution was bubbled with nitrogen gas to eliminate oxygen that could interfere with electrochemical measurements. Cyclic voltammetry was carried out using a CHI6284E potentiostat in a standard three-electrode configuration, with a clean gold macroelectrode serving as a working electrode. The potential was scanned from −0.6 V to 0.6 V at a scan rate of 50 mV s^{-1}, over three complete cycles (six segments). All the voltammograms are presented following the IUPAC convention, with anodic currents plotted as positive values on the *y*-axis and positive potentials to the right on the *x*-axis. The onset potential for hydrazine oxidation was observed around −0.424 ± 0.026 V *vs.* Ag|AgCl reference, marking the starting of its oxidation to nitrogen (Fig. 2e). In alkaline media, hydrazine undergoes a four-electron oxidation, yielding molecular N_2 as the final product.[16] This process is facilitated by the presence of hydroxyl ions (OH^-) in the solution, which participate in the electron transfer process upon applying potential.

The overall reaction for hydrazine oxidation in basic condition can be expressed by the following equation[22]

$$N_2H_4 + 4OH^- \rightarrow N_2 + 4H_2O + 4e^- \quad (1)$$

To evaluate the electrocatalytic properties of the ring electrodes, we performed cyclic voltammetry under similar conditions. The potential was scanned from −0.7 V and 0.6 V at 50 mV s^{-1} for two cycles (four segments). A distinct onset for

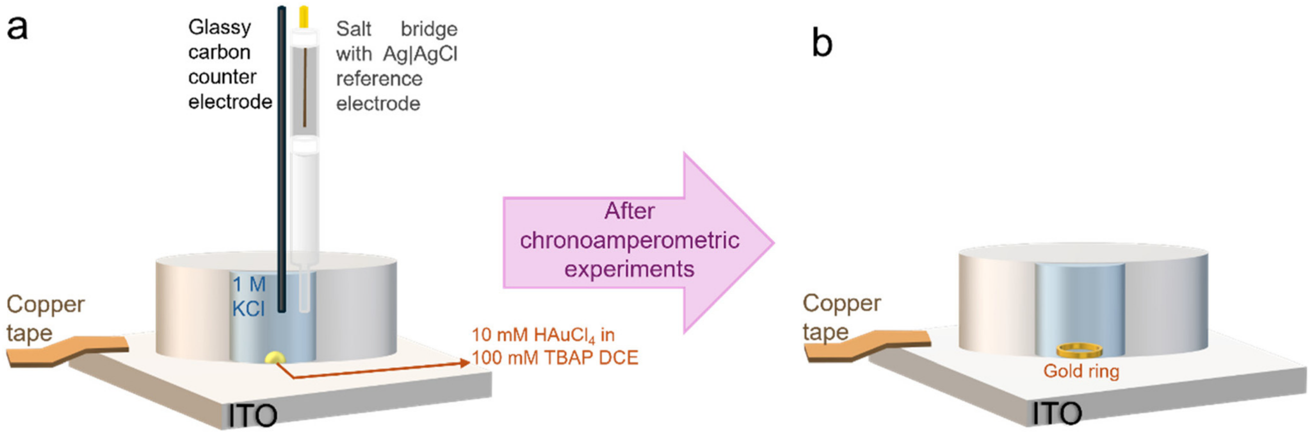

Fig. 1 (a) Schematic for ring deposition with a droplet (yellow) of 10 mM $HAuCl_4$ in 100 mM TBAP in DCE onto the ITO surface in the cell. A solution of 1 M KCl (blue) was used as the supporting electrolyte. Chronoamperometry was run from the potential −0.65 V for 0.5 s to 0.3 V for 0.5 s and cycled twice. (b) Schematic for the cell setup displaying the deposited gold nanoring at the interface of the ITO, droplet and supporting electrolyte phase.

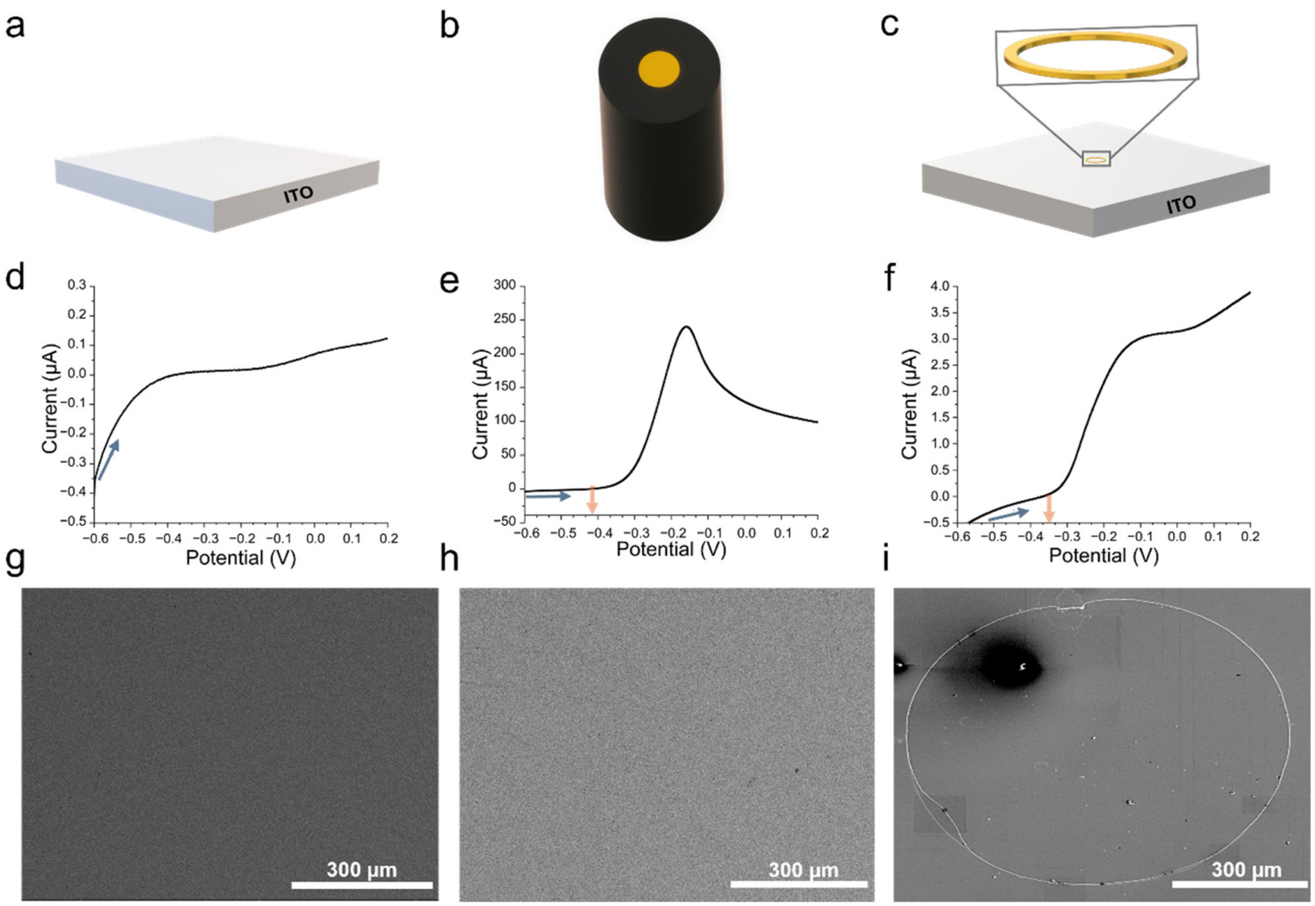

Fig. 2 (a), (b) and (c) show the schematic of the bare ITO, gold macroelectrode, and gold nanoring as electrodes, respectively. (d), (e), and (f) show cyclic voltammograms measured against Ag|AgCl (3M KCl) for hydrazine oxidation in 10 mM hydrazine in 250 mM KOH at 50 mV s^{-1}, scanned from −0.7 V to 0.6 V. Plots are shown up to 0.2 V for clarity, as no significant features appear beyond this range. Orange arrows indicate the onset potential for hydrazine oxidation. Scanning electrode microscope images of the surface of these electrodes are shown in (g), (h), and (i), respectively. Blue directional arrows indicate scan direction.

hydrazine oxidation was observed around −0.358 ± 0.048 V during the third segment (Fig. 2f), suggesting a shift in electrocatalytic behavior compared to the gold macroelectrode. Notably, the first cycle did not exhibit a pronounced onset dip (Fig. S4), an observation reproducible across multiple nanoring electrode samples. The area-normalized current density plot, presented in Fig. S5, corresponds to the data referenced in Fig. 2. This behavior may result from the initial stripping of loosely bound surface layers or contaminants during the first scan, effectively cleaning the nanoring surface and enabling catalytic activity in subsequent scans. The potential ranges and scan numbers were tailored to the electrodes' capacitive behaviors, with the macroelectrode showing clear oxidation in the first scan and the nanoring requiring chemical cleaning, making the third scan representative. A mild chemical cleaning method was used for the nanoring to avoid damage from aggressive electrochemical cleaning, which could strip the fragile ring from the ITO surface.[43] The onset potential was defined as the potential where the current exceeds the baseline capacitive current by >5%.[44]

Control experiments with a bare ITO substrate were performed under identical conditions. The cyclic voltammogram for bare ITO (Fig. 2d) showed negligible current response, confirming that ITO does not contribute significantly to hydrazine oxidation. This validates that the observed electrocatalytic activity arises solely from the gold ring present on the ITO substrate.

2.3. Simulation

To validate our experimental results, we modeled our system using finite element simulation in COMSOL Multiphysics 6.2, incorporating the precise dimensions of the active electrode surfaces: a gold macroelectrode and a single gold nanoring electrode. Fig. 3a presents the overlay of the experimental cyclic voltammogram (red trace) and simulated response (black trace) for the macroelectrode, demonstrating a good agreement between the two.

The bulk diffusion coefficient of hydrazine in an alkaline medium was determined experimentally using square-wave voltammetry to be 8.928×10^{-10} m^2 s^{-1}, consistent with

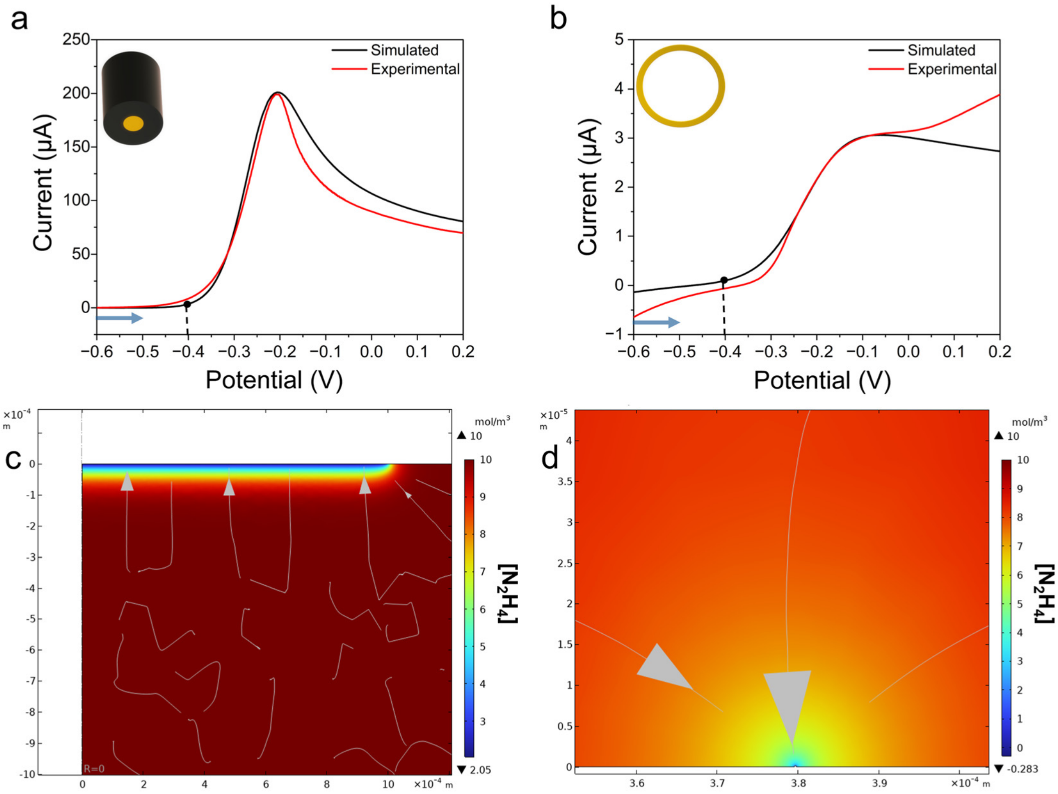

Fig. 3 Overlayed cyclic voltammograms of simulated data (black trace) and experimental data (red trace) are shown in (a) and (b) for a gold macroelectrode and the gold single nanoring, respectively. (c) Shows a concentration profile for hydrazine oxidation on the gold macroelectrode at 8 s, −0.44 V, (black dot) and (d) shows the concentration profile on the gold nanoring at 13.5 s, at −0.43 V. Blue directional arrows indicate scan direction.

literature values.[45,46] To account for geometry-dependent transport effects in the adsorption process, distinct diffusion coefficients were assigned to the adsorption layers at the electrode surfaces. For the macroelectrode, a 20 nm thick adsorption layer was modeled with a diffusion coefficient of 8.928×10^{-11} m^2 s^{-1}, reflecting the reduced mobility of hydrazine molecules in the adsorbed phase due to the broader, more diffuse interaction zone enabled by the larger electrode surface.[47] In contrast, the nanoring electrode was modeled with a 2 nm thick adsorption layer and a diffusion coefficient of 8.928×10^{-12} m^2 s^{-1}, capturing the tighter confinement of adsorbed species due to the nanoring's restricted geometry. These parameters were chosen to represent the interfacial kinetics and mass-transport phenomena in COMSOL simulations. The nanoring's 2 nm adsorption layer was assigned a diffusion coefficient of 8.928×10^{-12} m^2 s^{-1} to model enhanced radial diffusion due to its annular geometry, contrasting with the planar diffusion at the macroelectrode. For the macroelectrode, we employed Butler–Volmer kinetics with a rate constant of 0.002 cm s^{-1}, within the reported literature range, and a formal potential of −0.279 V. The simulated cyclic voltammogram closely matched the experimental data, as shown in Fig. 3a. The concentration profile of hydrazine consumption at 8 s is depicted in Fig. 3c.

Similarly, for the nanoring electrode, the simulation utilized Butler–Volmer kinetics with the same rate constant but a formal potential of −0.4 V, reflecting the sensitivity of hydrazine oxidation to local pH variations near the electrode surface. The cyclic voltammogram, shown in Fig. 3b, was simulated over a potential range of −0.7 V to −0.3 V, as the simulated trace exhibits different behavior beyond this range. The 2 nm adsorption layer with a diffusion coefficient of 8.928×10^{-12} m^2 s^{-1} was incorporated to model the confined adsorption dynamics. The observed differences in current response are attributed to local pH variations at the nanoring surface. Fig. 3d illustrates the concentration profile of hydrazine oxidation at 13.5 s, corresponding to the second anodic segment of the experimental data.

These tailored adsorption layer parameters ensure accurate modeling of electrochemical behavior influenced by electrode geometry, providing robust agreement with experimental results for both electrode types. The macroelectrode surface area was calculated as $A = \pi r^2$ using the manufacturer's radius. The nanoring's area was estimated as $A = \pi(r^2_{\text{outer}} - r^2_{\text{inner}})$, with radii derived from SEM-measured ring thickness. We

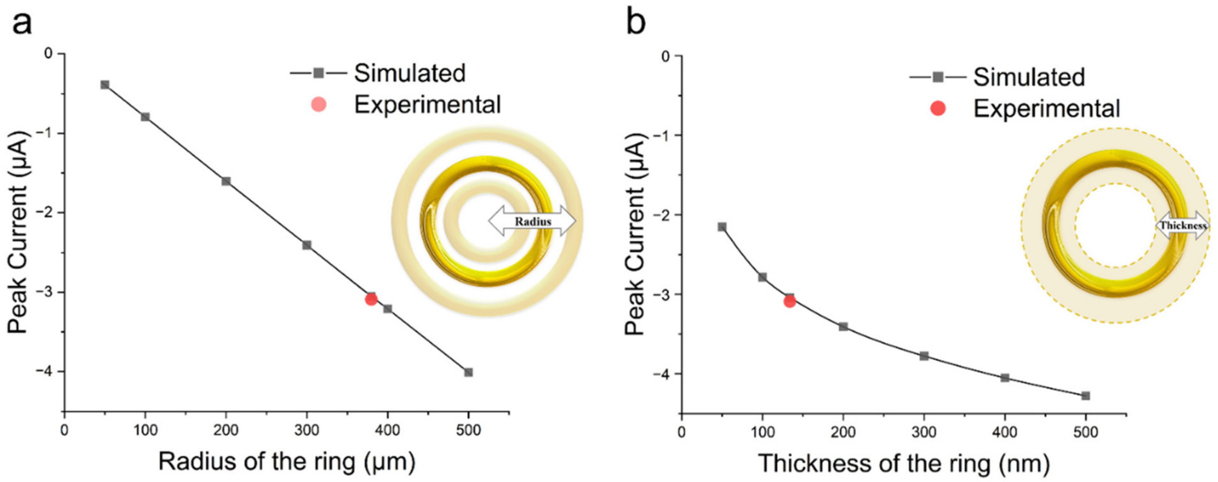

Fig. 4 (a) Shows the simulated trend (grey trace) of peak current with change of radius of the ring keeping the thickness constant (133.75 nm). (b) Shows the simulated peak current with change in the thickness of the ring while keeping the radius constant (379.65 μm). The experimental peak current value (red dot) obtained from the voltammogram is shown in both. (a) and (b) show experimental data for a single nanoring geometry due to computational limitations, though similar electrochemical responses were observed across multiple nanoring samples.

retained unnormalized currents in Fig. 2 and 3 to preserve the raw electrochemical responses, as normalization could mask absolute current differences critical for evaluating nanoring performance.

Source	Diffusion coefficient ($m^2\ s^{-1}$)	% Deviation from experimental value
This work	8.928×10^{-10}	—
Choudhry *et al.*, 2014[46]	8.550×10^{-10}	4.2
Choudhry *et al.*, 2014[46]	7.78×10^{-10}	12.8

The experimentally determined diffusion coefficient for hydrazine ($8.928 \times 10^{-10}\ m^2\ s^{-1}$) was compared to literature values. The table below summarizes the comparison and percentage deviation. The agreement was deemed good as the coefficient is within the similar order of magnitude as the cited values.

The diffusion mechanism varies with electrode geometry, significantly influencing the mass transport process. Studies by Zhong *et al.* and Ngamchuea *et al.* demonstrate that mass transport in macroelectrodes is primarily governed by linear diffusion from the supporting electrolyte solution to the electrode surface, leading to a stable current response characterized by a semi-infinite planar diffusion model.[32] In contrast, nanoring electrodes act like microbands, exhibiting a radial diffusion profile due to their nanometer-scale thickness.

A parametric sweep was run for different radii of the ring, keeping the thickness constant, and different thicknesses with a constant radius. The radius and thickness used for the simulation were derived from SEM images of the ring. Fig. 4 shows the corresponding peak current for the individual sweeps. A linear relationship with a negative slope is observed between the peak current and the radius of the ring, whereas the peak current is inversely related to the thickness of the ring. For the ring shown in Fig. 2(i), the experimental peak current value was plotted and shows good agreement with the simulated value of the corresponding radius or thickness in Fig. 4. The linear trend in Fig. 4 reflects a proportional increase in current with applied potential (−0.7 V to −0.3 V), consistent with diffusion-limited Butler–Volmer kinetics, driven by enhanced radial diffusion at the nanoring geometry, as validated by COMSOL simulations. While simulations explored various ring dimensions, experimental validation was conducted on a single nanoring geometry due to computational constraints, though similar electrochemical behavior was observed across multiple nanorings. To address reproducibility, hydrazine oxidation experiments on gold nanoring electrodes were conducted across six independently fabricated nanoring samples ($n = 6$), each prepared under identical electrodeposition conditions (1 M KCl electrolyte, −0.65 V *vs.* Ag|AgCl). The electrochemical responses were highly reproducible, with onset potential varying by less than 5% (mean onset: −0.358 ± 0.048 V), though peak currents varied due to differences in ring geometry or surface roughness, as reported in similar studies on nanostructured electrodes. Due to computational limits in COMSOL Multiphysics 6.2, simulations were run for one nanoring geometry (outer radius: 5 μm, thickness: 134 nm), with results closely matching experimental data.

3. Conclusion

In summary, we present a technique to fabricate a nanoscale electrode with ultra-high aspect ratio and demonstrate its electrocatalytic performance for hydrazine oxidation in alkaline medium. The nanoring electrodes, owing to their dimensions and radial diffusion characteristics, exhibit an onset potential similar to that of a gold macroelectrode. This is attributed to improved mass transport dynamics driven by the nanoring geometry. Theoretical modeling using COMSOL Multiphysics provided strong agreement with experimental results, offering mechanistic insights into electrochemical behavior. These findings highlight the potential of nanorings for broader applications, including sensors and energy conversion systems.

4. Materials and methods

4.1. Reagents and materials

Gold(III) chloride trihydrate ($HAuCl_4\ 3H_2O$, ≥99.9%), hydrazine (anhydrous, 98%), tetrabutylammonium perchlorate ($[NBu_4][ClO_4]$, 99% purity), and 1,2-dichloroethane (DCE, 99%) were purchased from Sigma-Aldrich. Potassium hydroxide (KOH) was obtained from Fischer Chemicals, and potassium chloride (KCl) was purchased from Fisher BioReagents. Microcloth polishing pads were obtained from Buehler, Lake Bluff and the alumina powder suspensions were acquired from Electron Microscopy Sciences, Hatfield. Millipore GenPure ultrapure water (18.20 MΩ cm) was used to prepare all the aqueous solutions. A 1 M potassium chloride was used as the aqueous supporting electrolyte. The 10 mM gold solution was prepared using a 100 mM solution of $[NBu_4][ClO_4]$ with DCE, and a 10 mM hydrazine solution was prepared using 250 mM aqueous KOH. The gold working macroelectrode (r = 1 mm) and Ag|AgCl reference electrode (stored in 1 M potassium chloride) were obtained from CH Instruments (Austin, TX), and the counter electrode was a glassy carbon rod (0.5 mm radius) from Thermo Fisher (Tewksbury, MA). A 1 cm square piece of indium tin oxide (ITO) conductive-coated glass was used as the working electrode with a 1.5 mm radius as the electroactive surface area. The working electrode (ITO) was thoroughly cleaned using ultrapure water and dried with an inert nitrogen gun. A salt bridge, made using a cooled solution of 3% agarose (99.9%, Sigma-Aldrich, Ward-Hill, MA) and 1 M KCl (Fisher Bioreagents, Fair Lawn, NJ), was used to connect the reference electrode to the solutions to reduce solvent effects on electrode behavior. The working macroelectrodes were thoroughly cleaned by polishing on a micro-cloth polishing pad with a slurry of 0.5 μm alumina suspension, followed by cleaning with Milli-Q water and ethanol, and further polished using a 0.03 μm alumina suspension and a clean micro-cloth polishing pad. All potentials are referenced to an Ag|AgCl (3 M KCl) electrode.

4.2. Electrochemical methods

All electrochemical experiments were performed on a CHI 601D and CHI 6384D potentiostat from CH Instruments using a three-electrode setup. A holder made of inert resin was used to run experiments on the ITO. A submicron volume of an organic solution containing 10 mM $HAuCl_4$ $3H_2O$ and $[NBu_4][ClO_4]$ in DCE was pipetted into the cell with ITO surface (r = 1.5 mm) and submerged in 3 mL of 1 M KCl supporting electrolyte solution. The working electrode surface was in contact with both the organic droplet and the supporting electrolyte aqueous solution simultaneously. The ITO was connected to the potentiostat *via* copper tape. The thin glassy carbon counter electrode and the salt bridge (connected to the reference electrode) were placed in the supporting electrolyte aqueous solution. Electrodeposition of the ring was performed using chronoamperometry with the CHI 601D potentiostat (Fig. S6). Some rings show gold particles deposited within, which may occur due to improper cleaning of the ITO surface prior to electrodeposition. Though the reproducibility of these nanorings appears to be low, similar current responses were observed for these rings. The rings were stable, and efforts are ongoing to increase reproducibility and optimization. The ITO surface was cleaned, and then a 10 mM hydrazine in 250 mM KOH was pipetted onto the ITO. Cyclic voltammetry was performed for two cycles between −0.7 V to 0.6 V. Similarly, the hydrazine oxidation reaction was studied on a clean gold macroelectrode and a bare ITO surface. All the optical images were obtained using a Leica DMi8 microscope from Leica Microsystems with a 40× objective and a C15440 OrcaFusionBT sCMOS camera. Scanning electron microscopy (SEM) images of the bare ITO, bare gold macroelectrode, and the gold nanoring were taken using Teneo VolumeScope (WSLR S050). A through-the-lens detector (TLD) was used for high vacuum imaging with high magnification and resolution. Images were taken at 5 kV and a 5 mm distance. Energy-dispersive X-ray spectroscopy data were gathered on an Oxford Instruments EDS with an INCA PentaFet-X3 Si(Li) detector.

4.3. Simulation

COMSOL Multiphysics 6.2, a finite element modeling software, was used to compare simulated voltammograms and validate experimental data. The simulation utilized the obtained thickness and radius of the gold nanoring and considered the flux and radial diffusion at the ring using Butler–Volmer kinetics to simulate the oxidation of hydrazine. A similar simulation for the gold macroelectrode was modeled. Full COMSOL reports can be found in SI.

Author contributions

Sakshi A. Ailawar – Formal analysis, investigation, visualization, writing (original draft), and writing (review and editing). Guillermo Colon-Quintana – Conceptualization, formal analysis, investigation, and validation. Thomas B. Clarke – Conceptualization, formal analysis, and investigation. Jeffrey E. Dick – Conceptualization, resources, supervision, and writing (final draft).

Conflicts of interest

The authors declare no conflict of interest.

Data availability

The data supporting this article have been included as part of the supplementary information (SI). Supplementary information is available. Complete COMSOL reports for the electrocatalytic behavior of both the gold macroelectrode and gold nanoring electrodes are available. See DOI: https://doi.org/10.1039/d5an00651a.

Acknowledgements

We would like to acknowledge support from the National Science Foundation Chemical Measurement and Imaging Program under grant number CHE-2403964.

References

1 M. R. Andrew, W. J. Gressler, J. K. Johnson, R. T. Short and K. Williams, *Engineering aspects of hydrazine-air fuel-cell power systems*, 1972, vol. 2.

2 Y. Yu, S. J. Lee, J. Theerthagiri, Y. Lee and M. Y. Choi, *Appl. Catal., B*, 2022, **316**, 121603.

3 N. V. Rees and R. G. Compton, *Energy Environ. Sci.*, 2011, **4**, 1255–1260.

4 Schmidt E and Wucherer E, *Hydrazine(s) vs. Nontoxic Propellants – Where Do We Stand Now?* European Space Agency, (Special Publication) ESA SP, 2004.

5 R. Aggarwal, I. Patel and P. Sharma, *Int. J. Latest Trends Eng. Technol.*, 2015, **6**(1).

6 L. J. M. J. Blomen and M. N. Mugerwa, *Fuel cell systems*, Springer Science & Business Media, 2013.

7 A. Abbaspour, A. Khajehzadeh and A. Ghaffarinejad, *J. Electroanal. Chem.*, 2009, **631**, 52–57.

8 L. Q. Ye, Z. P. Li, H. Y. Qin, J. K. Zhu and B. H. Liu, *J. Power Sources*, 2011, **196**, 956–961.

9 M. Hasanzadeh, G. Karim-Nezhad, N. Shadjou, B. Khalilzadeh, L. Saghatforoush, S. Ershad and I. Kazeman, *Chin. J. Chem.*, 2009, **27**, 638–644.

10 Y. Fukumoto, T. Matsunaga and T. Hayashi, *Electrocatalytic Activities of Metal Electrodes in Anodic Oxidation of Hydrazine in Alkaline Solution*, 1980.

11 B. E. Conway, *et al.*, *J. Electrochem. Soc.*, 1966, **113**, 1144.

12 C. Batchelor-McAuley, C. E. Banks, A. O. Simm, T. G. J. Jones and R. G. Compton, *Analyst*, 2006, **131**, 106–110.

13 D. L. Burke and L. M. Hurley, *J. Solid State Electrochem.*, 2002, **6**, 101–110.

14 Q. Yi and W. Yu, *J. Electroanal. Chem.*, 2009, **633**, 159–164.

15 S. Koçak and B. Aslişen, *Sens. Actuators, B*, 2014, **196**, 610–618.

16 K. Korinek, J. Koryta, M. Musilov and J. Heyrovskf, *Electro-Oxidation of Hydrazine on Mercury, Silver and Gold Electrodes in Alkaline Solutions**, 1968.

17 M. Honda and T. Kodera, *Electrochemical Behaviour of Hydrazine on Platinum in Alkaline Solution*, 1984.

18 L. D. Burke and K. J. O'Dwyer, *Mediation of Oxidation Reactions at Noble Metal Anodes by Low Levels of In Situ Generated Hydroxy Species*, 1989.

19 J. A. Harrison and Z. A. Khan, *The Oxidation of Hydrazine in Alkaline Solution at Platinum and Mercury*, 1970.

20 Q. Yi, L. Li, W. Yu, X. Liu, Z. Zhou and H. Nie, *Rare Met.*, 2010, **29**, 26–31.

21 M. Ikawa and E. E. Snell, *The Voltammetric Characteristics and Mechanism of Electrooxidation of Hydrazine*, 1954, vol. 76.

22 K. Asazawa, K. Yamada, H. Tanaka, M. Taniguchi and K. Oguro, *J. Power Sources*, 2009, **191**, 362–365.

23 M. G. Hosseini, M. M. Momeni and S. Zeynali, *Surf. Eng.*, 2013, **29**, 65–69.

24 J. R. Stetter, K. F. Blurton, I. A. M. Valentine and K. A. Tellefsen, *The Electrochemical Oxidation of Hydrazine and Methylhydrazine on Gold: Application to Gas Monitoring*, 1972, vol. 9.

25 S. Szpak, P. Stonehart and T. Katan, *Electrode Reactions of Hydrazine in Aqueous Solutions*, Pergamon Press Ltd, 1965, vol. 10.

26 D. A. Walsh, A. Ejigu, S. Muhammad and P. Licence, *ChemElectroChem*, 2014, **1**(1), 281–288.

27 A. Zabielaitė, A. Balčiūnaitė, D. Šimkūnaitė, J. Vaičiūnienė and A. Selskis, Investigation of sodium borohydride and hydrazine oxidation on gold nanoparticles modified zinc-cobalt coating, *Chemija*, 2019, **30**, DOI: 10.6001/chemija.v30i3.4048.

28 X. Gao, J. Jang and S. Nagase, *J. Phys. Chem. C*, 2010, **114**, 832–842.

29 B. Álvarez-Ruiz, R. Gómez, J. M. Orts and J. M. Feliu, *J. Electrochem. Soc.*, 2002, **149**, D35.

30 R. Liu, Y. Luan, S. Sheng, B. Lin and J. Yin, *Chem. Lett.*, 2024, **53**, upae188.

31 S. Jia, L. Zhang, H. Liu, R. Wang, X. Jin, L. Wu, X. Song, X. Tan, X. Ma, J. Feng, Q. Zhu, X. Kang, Q. Qian, X. Sun and B. Han, *Nat. Commun.*, 2024, **15**, 8567.

32 K. Ngamchuea, S. Eloul, K. Tschulik and R. G. Compton, *J. Solid State Electrochem.*, 2014, **18**, 3251–3257.

33 H. Liu, Y. Liu, M. Li, X. Liu and J. Luo, *Mater. Today Adv.*, 7, DOI: 10.1016/j.mtadv.2020.100083.

34 G. Wang, S. Jing and Y. Tan, *Sci. Rep.*, 2017, **7**(1), DOI: 10.1038/s41598-017-16776-6.

35 *COMSOL Multiphysics® v6.2*.

36 AB. COMSOL, *COMSOL Multiphysics® User's Guide, Version 5.3a, COMSOL AB*, Stockholm, Sweden, pp. 1998–2017.

37 T. B. Clarke, G. S. Colón and J. E. Dick, *Adv. Mater. Technol.*, 2023, **8**(13), DOI: 10.1002/admt.202201946.

38 G. S. Colón-Quintana, T. B. Clarke and J. E. Dick, *Nat. Commun.*, 2023, **14**(1), DOI: 10.1038/s41467-023-35964-9.

39 G. Colón Quintana, T. Clarke, S. A. Ailawar and J. E. Dick, *Nanoscale*, 2024, **16**(43), 20073–20081.

40 A. Minenkov, S. Hollweger, J. Duchoslav, O. Erdene-Ochir, M. Weise, E. Ermilova, A. Hertwig and M. Schiek, *ACS Appl. Mater. Interfaces*, 2024, **16**, 9517–9531.

41 L. H. Mendoza-Huizar, *J. Solid State Electrochem.*, 2025, **29**, 1849–1861.

42 L. Wang, W. Mao, D. Ni, J. Di, Y. Wu and Y. Tu, *Electrochem. Commun.*, 2008, **10**, 673–676.

43 X. Deng, F. Galli and M. T. M. Koper, *J. Am. Chem. Soc.*, 2018, **140**, 13285–13291.

44 A. J. Bard and L. R. Faulkner, *Electrochemical methods: fundamentals and applications*, John Wiley & Sons, Inc., 2001.

45 D. T. Kallikragas, K. I. Choudhry, A. Y. Plugatyr and I. M. Svishchev, *J. Chem. Phys.*, 2013, **139**(13), DOI: **10.1063/1.4823513**.

46 K. I. Choudhry, I. M. Svishchev and A. Plugatyr, *Can. J. Chem.*, 2014, **92**, 279–283.

47 M. Stephen, M. Wood and B. Zhang, *Anal. Chem.*, 2013, **85**(2), 473–486.